

Reinventing 2D Convolutions for 3D Images

Jiancheng Yang*, Xiaoyang Huang*, Bingbing Ni**, Jingwei Xu, Canqian Yang, and Guozheng Xu

Shanghai Jiao Tong University
{jekyl14168, 13802896410, nibingbing, xjwxjw, charles.young, guozhengxu}@sjtu.edu.cn

Abstract. There have been considerable debates over 2D and 3D representation learning on 3D medical images. 2D approaches could benefit from large-scale 2D pretraining, whereas they are generally weak in capturing large 3D contexts. 3D approaches are natively strong in 3D contexts, however few publicly available 3D medical dataset is large and diverse enough for universal 3D pretraining. Even for hybrid (2D + 3D) approaches, the intrinsic disadvantages within the 2D / 3D parts still exist. In this study, we bridge the gap between 2D and 3D convolutions by reinventing the 2D convolutions. We propose ACS (axial-coronal-sagittal) convolutions to perform natively 3D representation learning, while utilizing the pretrained weights on 2D datasets. In ACS convolutions, 2D convolution kernels are split by channel into three parts, and convoluted separately on the three views (axial, coronal and sagittal) of 3D representations. Theoretically, **ANY** 2D CNN (ResNet, DenseNet, or DeepLab) is able to be converted into a 3D ACS CNN, with pretrained weight of a same parameter size. Extensive experiments on proof-of-concept dataset and several medical benchmarks validate the consistent superiority of the pretrained ACS CNNs, over the 2D / 3D CNN counterparts with / without pretraining. Even without pretraining, the ACS convolution can be used as a plug-and-play replacement of standard 3D convolution, with smaller model size and less computation.

Keywords: 3D medical images, ACS convolutions, transfer learning.

1 Introduction

Emerging deep learning technology has been dominating the medical image analysis research [39,55], in a wide range of data modalities (*e.g.*, ultrasound [7,17], CT [52,66,5], MRI [43,15,4], X-Ray [61,31,33]) and tasks (*e.g.*, classification [22,18], segmentation [32,59], detection [65,60], registration [2,12]). Thanks to contributions from dedicated researchers from academia and industry, there have been much larger medical image datasets than ever before. With large-scale datasets, strong infrastructures and powerful algorithms, numerous challenging

* Equal contribution.

** Corresponding author.

	2D Convolutions	3D Convolutions	Hybrid (2D +3D)	ACS Convolutions
Pros	2D pretrained weights on large 2D datasets	Natively 3D representations	2D + 3D representations	a. Natively 3D representations b. 3D pretrained weights on large 2D datasets c. Converting ANY 2D model into a single 3D model
Cons	Natively 2D representations	Lack of 3D pretrained weights on large datasets	a. 2D representation within 2D parts b. Lack of 3D pretrained weights c. Redundant multi-stage / multi-stream models	

Fig. 1: A comparison between the proposed ACS convolutions and prior art on modeling the 3D medical images: pure 2D / 2.5D approaches with 2D convolution kernels, pure 3D approaches with 3D convolution kernels, and hybrid approaches with both 2D and 3D convolution kernels. The ACS convolutions run multiple 2D convolution kernels among the three views (axial, coronal and sagittal).

problems in medical images seem solvable. However, the data-hungry nature of deep learning limits its applicability in various real-world scenarios with limited annotations. Compared to millions (or even billions) of annotations in natural image datasets, the medical image datasets are not large enough. Especially for 3D medical images, datasets with thousands of supervised training annotations [54,68,57] are so-called “large”, due to several difficulties in medical annotations: hardly-accessible and high dimensional medical data, expensive expert annotators (radiologists / clinicians), and severe class-imbalance issues [64].

Transfer learning, with pretrained weights from large-scale datasets (*e.g.*, ImageNet [13], MS-COCO [38]), is a de-facto paradigm for tasks with insufficient data. Unfortunately, widely-used pretrained CNNs are developed on 2D datasets, which are non-trivial to transfer to 3D medical images. Prior art on 3D medical images follows either 2D-based approaches or 3D-based approaches (compared in Fig. 1). 2D-based approaches [53,67,45] benefit from large-scale pretraining on 2D natural images, while the 2D representation learning are fundamentally weak in large 3D contexts. 3D-based approaches [11,44,69] learn natively 3D representations. However, few publicly available 3D medical dataset is large and diverse enough for universal 3D pretraining. Therefore, compact network design and sufficient training data are essential for training the 3D networks from scratch. Hybrid (2D + 3D) approaches [36,62,70] seem to combine the best of both worlds, nevertheless these ensemble-like approaches do not fundamentally overcome the intrinsic issues of 2D-based and 3D-based approaches. Please refer to Sec. 2 for in-depth discussion on these related methods.

There has been considerable debates over 2D and 3D representation learning on 3D medical images: prior studies choose either large-scale 2D pretraining or natively 3D representation learning. This paper presents an alternative to bridge the gap between the 2D and 3D approaches. To solve the intrinsic disadvantages from the 2D convolutions and 3D convolutions in modeling 3D images, we argue that an ideal method should adhere to the following principles:

- 1) ***Natively 3D representation***: it learns natively 3D representations;
- 2) ***2D weight transferable***: it benefits from large-scale 2D pretraining;
- 3) ***ANY model convertible***: it enables any 2D model, including classification, detection and segmentation backbones, to be converted to a 3D model.

These principles cannot be achieved simultaneously with standard 2D convolutions or standard 3D convolutions, which directs us to develop a novel convolution operator. Inspired from the widely-used tri-planar representations of 3D medical images [53], we propose *ACS convolutions* satisfying these three principles. Instead of explicitly treating the input 3D volumes as three orthogonal 2D planar images [53] (axial, coronal and sagittal), we operate on the convolution kernels to perform view-based 3D convolutions, via splitting the 2D convolution kernels into three parts by channel. Notably, **no additional 3D fusion layer** is required to fuse the three-view representations from the 3D convolutions, since they will be seamlessly fused by the subsequent ACS convolution layers (Sec. 3).

The ACS convolution aims at a generic and plug-and-play replacement of standard 3D convolutions for 3D medical images. Even without pretraining, the ACS convolution is comparable to 3D convolution with a smaller model size and less computation. When pretrained on large 2D datasets, it consistently outperforms 2D / 3D convolution by a large margin. To improve research reproducibility, a PyTorch [46] reference implementation of ACS convolution is provided in the supplementary materials. Using the provided function, 2D CNNs could be converted into ACS CNNs for 3D images, with a single line of code. It introduces no additional computation costs, in terms of FLOPs, memory and model size.

2 Related Work on 3D Medical Images

2.1 2D / 2.5D Approaches

Transfer learning from 2D CNNs, trained on large-scale datasets (*e.g.*, ImageNet [13]), is a widely-used approach in 3D medical image analysis. To mimic the 3-channel image representation (*i.e.*, RGB), prior studies follow either multi-planar or multi-slice representation of 3D images as 2D inputs. In these studies, pretrained 2D CNNs are usually fine-tuned on the target medical dataset.

Early study [48,53] proposes tri-planar representation of 3D medical images, where three views (axial, coronal and sagittal) from a voxel are regarded as the three channels of 2D input. Although this method is empirically effective, there is a fundamental flaw that the channels are not spatially aligned. More studies follow tri-slice representations [14,67,45], where a center slice together with its two neighbor slices are treated as the three channels. In these representations, the channels are spatially aligned, which conforms to the inductive biases in convolution. There are also studies [67,47] combining both multi-slice and multi-planar approaches, using multi-slice 2D representations in multiple views. The multi-view representations are averaged [67] or fused by additional networks [47].

Even though these approaches benefit from large-scale 2D pretraining, which is empirically effective in numerous studies [42,18,37,8], both multi-slice and

multi-planar representation with 2D convolutions are fundamentally weak in capturing large 3D contexts.

2.2 3D Approaches

Instead of regarding the 3D spatial information as input channels in 2D approaches, there are numbers of studies using pure 3D convolutions for 3D medical image analysis [11,44,34,16,69]. Compared to limited 3D contexts along certain axis in 2D approaches, the 3D approaches are theoretically capable of capturing arbitrarily large 3D contexts in any axis. Therefore, the 3D approaches are generally better at tasks requiring large 3D contexts, *e.g.*, distinguishing small organs, vessels, and lesions.

However, there are also drawbacks for pure 3D approaches. One of the most important is the lack of large-scale universal 3D pretraining. For this reason, efficient training of 3D networks is a pain point for 3D approaches. Several techniques are introduced to (partially) solve this issue, *e.g.*, deep supervision [16], compact network design [71,69]. Nevertheless, these techniques are not directly targeting the issue of 3D pretraining.

A related study of our method is Parallel Separable Convolution (PSC) [21], which extends pseudo 3D convolution (P3D) [49] in multiple parallel streams of various directions. Both introduce additional layers apart from 2D convolutions, thereby not all weights could be pretrained. As a comparison, our approach converts whole pretrained network seamlessly, while keeping same computation as the 2D variants, in terms of FLOPs, memory and parameters (Table 2).

2.3 Hybrid Approaches

Hybrid approaches are proposed to combine the advantages of both 2D and 3D approaches [36,62,70,47]. In these studies, 2D pretrained networks with multi-slice inputs, and 3D randomly-initialized networks with volumetric inputs are (jointly or separately) trained for the target tasks.

The hybrid approaches could be mainly categorized into multi-stream and multi-stage approaches. In multi-stream approaches [36,70], 2D networks and 3D networks are designed to perform a same task (*e.g.*, segmentation) in parallel. In multi-stage (*i.e.*, cascade) approaches [62,70,47], several 2D networks (and 3D networks) are developed to extract representations from multiple views, and a 3D fusion network is then used to fuse the multi-view representations into 3D representations to perform the target tasks.

Although empirically effective, the hybrid approaches do not solve the intrinsic disadvantages of 2D and 3D approaches: the 2D parts are still not able to capture large 3D contexts, and the 3D parts still lacks large-scale pretraining. Besides, these ensemble-like methods are generally redundant to deploy.

2.4 Transfer Learning and Self-Supervised Learning

Medical annotations require expertise in medicine and radiology, which are thereby expensive to be scalable. For certain rare diseases or novel applications

Source	Scale Diversity		Supervised Medical		2D CNNs	ACS CNNs
2D Image	***	***	Y	N	Conv2D $K \times K$	ACSCConv $K \times K$
Video [24]	**	**	Y	N	Conv2D 1×1	Conv3D $1 \times 1 \times 1$
Med3D [9]	*	*	Y	Y	Norm2D	Norm3D
MG [72]	**	*	N	Y	Pool2D	Pool3D

Table 1: **Left:** A comparison of transfer learning for 3D medical images from various sources, in terms of data scale, data diversity, whether supervised pre-training and whether medical data. **Right:** Main operator conversion from 2D CNNs into ACS CNNs. $K \times K$, 1×1 and $1 \times 1 \times 1$ denote the kernel sizes.

(*e.g.*, predicting response for novel treatment [58]), the data scale is naturally very small. Transfer learning from large-scale datasets to small-scale datasets is a de-facto paradigm in this case.

Human without any radiological experience could recognize basic anatomy and lesions on 2D and 3D images with limited demonstration. Based on this observation, we believe that transfer learning from universal vision datasets (*e.g.*, ImageNet [13], MS-COCO [38]) should be beneficial for 3D medical image analysis. Although there is literature reporting that universal pretraining is useless for target tasks [25,50], this phenomenon is usually observed when target datasets are large enough. Apart from boosting task performance, the universal pretraining is expected to improve model robustness and uncertainty quantification [28].

Unfortunately, 2D-to-3D transfer learning has not been adequately studied. Research efforts [34,20] have been paid to pretrain natively 3D CNNs on 3D datasets, however few publicly available 3D medical dataset is large and diverse enough for universal pretraining. Prior research explores the transfer learning of 3D CNNs trained on spatio-temporal video datasets [30]. However, there are two kinds of domain shift between video and 3D medical images: 1) natural images vs. medical images, and 2) spatio-temporal data vs. 3D spatial data. The domain shift makes video pretraining [24] less applicable for 3D medical images. To reduce domain shift, there is research (Med3D [9]) building pretrained 3D models on numbers of 3D medical image datasets. Despite the tremendous effort on collecting data from multiple sources, the data scale of involved 1,000+ training samples is still too much small compared to 1,000,000+ training samples in natural image datasets.

In addition to supervised pretraining, Models Genesis [72] explores unsupervised (self-supervised) learning to obtain the pretrained 3D models. Though very impressive, the model performance of up-to-date unsupervised learning is generally not comparable to that of fully supervised learning; even *state-of-the-art* unsupervised / semi-supervised learning techniques [3,27] could not reproduce the model performance using fully supervised training data.

Table 1 (Left) compares the sources of transfer learning for 3D medical images. Compared to transfer learning from video [24] / Med3D [9] / Models Genesis [72], the key advantage of 2D image pretraining is the *overwhelming* data

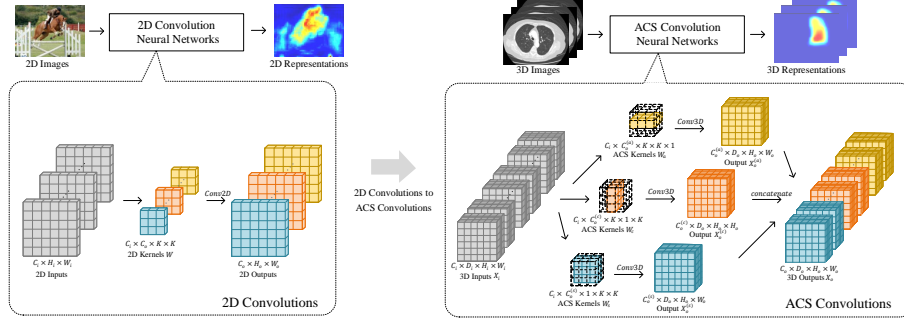


Fig. 2: Illustration of ACS convolutions and 2D-to-ACS model conversion. With a kernel-splitting design, a 2D convolution kernel could be seamlessly transferred into ACS convolution kernels to perform natively 3D representation learning. The ACS convolutions enable **ANY** 2D model (ResNet [26], DenseNet [29], or DeepLab [8]) to be converted into a 3D model.

scale and diversity of datasets. With the ACS convolutions proposed in this study, we are able to develop natively 3D CNNs using 2D pretrained weights. We compare these pretraining approaches in our experiments, and empirically prove the superiority of the proposed ACS convolutions.

Note that the contribution of the ACS convolutions is orthogonal to pre-training data. It is possible to pretrain ACS CNNs on 2D images, videos and 3D medical images with supervised / self-supervised learning. This paper uses ACS convolutions with supervised pretraining on 2D natural images to demonstrate the effectivity, flexibility and versatility.

3 ACS Convolutional Neural Networks

3.1 ACS Convolutions

Convolution layers capture spatial correlation. Intuitively, the formal difference between 2D and 3D convolutions is the kernel size: the 2D convolutions use 2D kernels ($C_o \times C_i \times K \times K$) for 2D inputs ($C_i \times H_i \times W_i$), whereas the 3D convolutions use 3D kernels ($C_o \times C_i \times K \times K \times K$) for 3D inputs ($C_i \times D_i \times H_i \times W_i$), where C_i , C_o denote the channels of inputs and outputs, K denotes the kernel size, and $(D_i \times)H_i \times W_i$ denotes the input size. To transfer the 2D kernels to 3D kernels, there are basically two prior approaches: 1) “inflate” the pretrained 2D kernels into 3D kernels size ($K \times K \rightarrow K \times K \times K$), *i.e.*, Inflated 3D (I3D [6]), where the 2D kernels are repeated along an axis and then normalized; 2) unsqueeze the 2D kernels into pseudo 3D kernels on an axis ($K \times K \rightarrow 1 \times K \times K$), *i.e.*, AH-Net-like [41], which could not effectively capture 3D contexts. Note that in both cases, the existing methods assume a specific axis to transfer the 2D kernels. It is meaningful to assign a special axis for spatio-temporal videos, while

controversial for 3D medical images. Even for anisotropic medical images, *any view of a 3D image is still a 2D spatial image*.

Based on this observation, we develop ACS (axial-coronal-sagittal) convolutions to learn spatial representations from the axial, coronal and sagittal views. Instead of treating channels of 2D kernels identically [6,41], we split the kernels into three parts for extracting 3D spatial information from the axial, coronal and sagittal views. The detailed calculation of ACS convolutions is shown in the supplementary materials. For simplicity, we introduce ACS convolutions with same padding (Fig. 2).

Given a 3D input $\mathbf{X}_i \in \mathbb{R}^{C_i \times D_i \times H_i \times W_i}$, we would like to obtain a 3D output $\mathbf{X}_o \in \mathbb{R}^{C_o \times D_o \times H_o \times W_o}$, with pretrained / non-pretrained 2D kernels $\mathbf{W} \in \mathbb{R}^{C_o \times C_i \times K \times K}$. Here, C_i and C_o denote the input and output channels, $D_i \times H_i \times W_i$ and $D_o \times H_o \times W_o$ denote the input and output sizes, K denotes the kernel size. Instead of presenting 3D images into tri-planar 2D images [53], we split and reshape the kernels into three parts (named ACS kernels) by the output channel, to obtain the view-based 3D representations for each volume: $\mathbf{W}_a \in \mathbb{R}^{C_o^{(a)} \times C_i \times K \times K \times 1}$, $\mathbf{W}_c \in \mathbb{R}^{C_o^{(c)} \times C_i \times K \times 1 \times K}$, $\mathbf{W}_s \in \mathbb{R}^{C_o^{(s)} \times C_i \times 1 \times K \times K}$, where $C_o^{(a)} + C_o^{(c)} + C_o^{(s)} = C_o$. It is theoretically possible to assign an ‘‘optimal axis’’ for a 2D kernel; However, considering the feature redundancy in CNNs [23], in practice we simply set $C_o^{(a)} \approx C_o^{(c)} \approx C_o^{(s)} \approx \lfloor C_o/3 \rfloor$. We then compute the axial, coronal and sagittal view-based 3D features via 3D convolutions:

$$\mathbf{X}_o^{(a)} = \text{Conv3D}(\mathbf{X}_i, \mathbf{W}_a) \in \mathbb{R}^{C_o^{(a)} \times D_o \times H_o \times W_o}, \quad (1)$$

$$\mathbf{X}_o^{(c)} = \text{Conv3D}(\mathbf{X}_i, \mathbf{W}_c) \in \mathbb{R}^{C_o^{(c)} \times D_o \times H_o \times W_o}, \quad (2)$$

$$\mathbf{X}_o^{(s)} = \text{Conv3D}(\mathbf{X}_i, \mathbf{W}_s) \in \mathbb{R}^{C_o^{(s)} \times D_o \times H_o \times W_o}. \quad (3)$$

The output feature \mathbf{X}_o is obtained by concatenating $\mathbf{X}_o^{(a)}$, $\mathbf{X}_o^{(c)}$ and $\mathbf{X}_o^{(s)}$ by the channel axis. It is noteworthy that, **no 3D fusion layer is required additionally**. The view-based output features will be automatically fused by subsequent convolution layers, without any additional operation, since the convolution kernels are **not** split by input channel. Thanks to linearity of convolutions, expectation of features from converted ACS convolutions keeps the same as that of 2D ones, thereby no weight rescaling [6] is needed. It is also the prerequisite for the usefulness of 2D pretraining in the converted ACS convolutions. The ACS convolution could learn strong 3D representations, since it could be regarded as a special case of 3D convolution, where the kernels are block sparse.

The proposed method enables ANY 2D model to be converted into a 3D model. Table 1 (Right) lists how operators in 2D CNNs are converted to those in ACS CNNs. Note that the converted models could load the 2D weights directly.

3.2 Counterparts and Related Methods

2D Convolutions. We include a simple AH-Net-like [41] 2D counterpart, by replacing all ACS convolutions in ACS CNNs with Conv3D $1 \times K \times K$. We name this pseudo 3D counterpart as ‘‘2.5D’’ in our experiments, which enables 2D pretrained weight transferring with ease.

Kernels	FLOPs	Memory	Parameters
Conv2D	$\mathcal{O}(DHW C_o C_i K^2)$	$DHWC_o$	$C_o C_i K^2$
Conv3D	$\mathcal{O}(DHW C_o C_i K^3)$	$DHWC_o$	$C_o C_i K^3$
ACSCConv	$\mathcal{O}(DHW C_o C_i K^2)$	$DHWC_o$	$C_o C_i K^2$
M-ACSCConv	$\mathcal{O}(3DHW C_o C_i K^2)$	$3DHWC_o$	$C_o C_i K^2$
S-ACSCConv	$\mathcal{O}(3DHW C_o C_i K^2)$	$3DHWC_o$	$C_o(C_i K^2 + 3)$

Table 2: Space and time complexity analysis, for 2D (2.5D), 3D, ACS, Mean-ACS, and Soft-ACS convolutions. Bias terms are not counted in parameters.

3D Convolutions. For the 3D counterparts, we replace all convolutions in ACS CNNs with standard 3D convolutions. Various pretraining sources (I3D [6] with 2D images, Med3D [9], Video [24]) are included for fair comparison. If there is any difference between the converted 3D models and the pretrained 3D models, we keep the pretrained 3D network architectures to load the pretrained weights. Models Genesis [72] uses 3D UNet-based [11,44] network architecture. We train the same network from scratch / with its self-supervised pretraining to compare with our models. Moreover, we implement P₃SC₁ to compare Parallel Separable Convolutions [21] with ACS convolutions. The P₃SC₁ models are trained from scratch due to the lack of pretraining with this method [21].

Table 2 compares the time and space complexity of 2D (2.5D), 3D and ACS convolutions. The proposed ACS convolution could be used as a generic and plug-and-play replacement of 3D convolution, with less computation and smaller size. Besides, the ACS convolution enables 2D pretraining. We demonstrate its superiority over the counterparts with extensive experiments (Sec. 4).

3.3 ACS Convolution Variants

Apart from the kernel splitting approach used in the proposed ACS convolutions, there are possible variants to implement the 2D-transferable ACS convolutions.

Mean-ACS convolutions. Instead of splitting the 2D convolution kernels, we replicate and reshape \mathbf{W} into $\mathbf{W}'_a \in \mathbb{R}^{C_o \times C_i \times K \times K \times 1}$, $\mathbf{W}'_c \in \mathbb{R}^{C_o \times C_i \times K \times 1 \times K}$, $\mathbf{W}'_s \in \mathbb{R}^{C_o \times C_i \times 1 \times K \times K}$, and obtain the 3D features $\mathbf{X}'_o^{(a)} = \text{Conv3D}(\mathbf{X}_i, \mathbf{W}'_a)$, $\mathbf{X}'_o^{(c)} = \text{Conv3D}(\mathbf{X}_i, \mathbf{W}'_c)$, $\mathbf{X}'_o^{(s)} = \text{Conv3D}(\mathbf{X}_i, \mathbf{W}'_s)$. The output features is

$$\mathbf{X}_o^M = (\mathbf{X}'_o^{(a)} + \mathbf{X}'_o^{(c)} + \mathbf{X}'_o^{(s)})/3. \quad (4)$$

Soft-ACS convolutions. Note that the Mean-ACS convolution uses a symmetric aggregation, thereby it could not distinguish any view-based information. To this regard, we introduce weighted sum of Mean-ACS, *i.e.*, Soft-ACS,

$$\mathbf{X}_o^S = \alpha^{(a)} \mathbf{X}'_o^{(a)} + \alpha^{(c)} \mathbf{X}'_o^{(c)} + \alpha^{(s)} \mathbf{X}'_o^{(s)}, \quad (5)$$

where $\alpha^{(a)}, \alpha^{(c)}, \alpha^{(s)} \in \mathbb{R}$ are learnable weights.

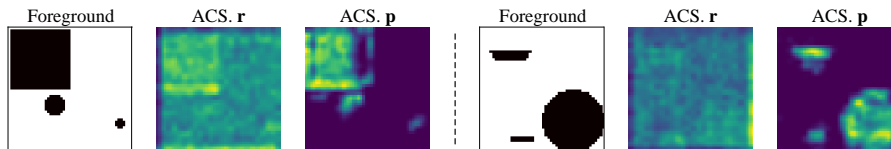


Fig. 3: Examples of (single-slice) features from ACS **r.** and **p.** on the 3D dataset **without** any training on it. ACS **p.** is pretrained on the 2D dataset.

In Table 2, we compare the time and space complexity. The two variants are more computationally intensive in terms of FLOPs and memory. Unfortunately, they do not provide significant performance boost empirically. Therefore, we only report the model performance of ACS convolutions in Sec. 4, and analyze these variants in Sec. 5.1.

4 Experiments

We experiment with the proposed method on a proof-of-concept dataset and medical benchmarks. To fairly compare model performance, we include several counterparts (2.5D/3D/ACS {Network} **r./p.**) with the same experiment setting, where **r.** denotes random initialization, and **p.** denotes pretraining on various sources. We use separate network architectures in different experiments to demonstrate the flexibility and versatility of the proposed method.

4.1 Proof of Concept: How Does the Pretraining Work?

Motivation. We would like to intuitively understand whether the 2D pretraining could be useful for the converted ACS models. For this reason, we design a proof-of-concept experiments with a synthetic dataset, where the “knowledge” from the 2D space is guaranteed to be useful in the 3D space. UNet-based models [51,11] segment the foregrounds, on the dataset consisting of sufficient 2D samples (foreground: circle and square) for pretraining the 2D networks and limited 3D samples (foreground: sphere, cube, cylinder, cone and pyramid) for evaluating the converted ACS networks. Note that the shapes of 2D dataset are exactly the projected single views of 3D volumes (except for triangle), thereby the 2D pretraining is expected to be useful in the 3D segmentation. We quantitatively analyze feature discriminative ability on the 3D dataset **without** training on it, using a mAUC metric based on ROC analysis [19] of final layer features to discriminate the foreground. We then train the UNets and compare the ACS, 2.5D and 3D counterparts. Dice and mIoU averaged on the 5 foreground classes are reported on the 3D dataset. Details of the synthetic dataset, network, training and mAUC metric are provided in the supplementary materials.

Result Analysis. We first illustrate two examples of feature maps from ACS **r.** and ACS **p.** on the 3D dataset in Fig. 3. Even without any training on the target

Models	Feature mAUC w/o training	Dice	mIoU	Model Size
2.5D UNet r.	69.0	82.2	72.5	1.6 Mb
2.5D UNet p.	85.1	82.7	73.3	1.6 Mb
3D UNet r.	72.1	94.6	90.8	4.7 Mb
ACS UNet r.	68.7	94.7	90.7	1.6 Mb
ACS UNet p.	88.1	95.4	92.0	1.6 Mb

Table 3: Segmentation performance of 2.5D, 3D and ACS convolution models w/ and w/o pretraining on the proof-of-concept dataset. **r.** denotes randomly initialized. The 2.5D and ACS UNet **p.** are pretrained on synthetic 2D images.

dataset, the features from ACS **p.** are well aligned with the foreground. As shown in Table 3, the mAUC metric of ACS **p.** is significantly higher than ACS **r.**, which empirically proves the usefulness of pretraining for ACS convolutions. Notably, features from ACS **p.** are even more discriminative than 2.5D **p.** After training on the 3D dataset, the performance of ACS UNet **r.** is comparable to 3D UNet **r.**, and the ACS UNet **p.** achieves the best performance. The results indicate that ACS convolution is an alternative to 3D convolution with comparable or even better performance, and a smaller model size.

4.2 Lung Nodule Classification and Segmentation

Dataset. We then validate the effectiveness of the proposed method on a large medical data LIDC-IDRI [1], the largest public lung nodule dataset, for both lung nodule segmentation and malignancy classification task. There are 2,635 lung nodules annotated by at most 4 experts, from 1,018 CT scans. The annotations include pixel-level labelling of the nodules and 5-level classification of the malignancy, from “1” (highly benign) to “5” (highly malignant). For segmentation, we choose one of the up to 4 annotations for all cases. For classification, we take the mode of the annotations as its category. In order to reduce ambiguity, we ignore nodules with level-“3” (uncertain labelling) and perform binary classification by categorizing the cases with level “1/2”, “4/5” into class 0, 1. It results in a total of 1,633 nodules for classification. We randomly divide the dataset into 4 : 1 for training and evaluation, respectively. At training stage we perform data augmentation including random-center cropping, random-axis rotation and flipping.

Experiment Setting. We compare the ACS models with 2.5D and 3D counterparts with or without pretraining. The pretrained 2.5D / ACS weights are from PyTorch’s torchvision package [46], trained on ImageNet [13]. For 3D pretraining, we use the official pretrained models by Med3D [9] and Video[24], while I3D [6] weights are transformed from the 2D ImageNet-pretrained weights as well. For PSC [21], we use the configuration of P₃SC₁, which resembles our ACS methods. To take advantage of the pretrained weights from Med3D [9] and video

Models	Segmentation (Dice)	Classification (AUC)
Models Genesis [72] r.	75.5	94.3
Models Genesis [72] p.	75.9	94.1
P ₃ SC ₁ [21] r.	74.3	90.9
2.5D Res-18 r.	68.8	89.4
2.5D Res-18 p.	69.8	92.0
3D Res-18 r.	74.7	90.3
3D Res-18 p. I3D [6]	75.7	91.5
3D Res-18 p. Med3D [9]	74.9	90.6
3D Res-18 p. Video [24]	75.7	91.0
ACS Res-18 r.	75.1	92.5
ACS Res-18 p.	76.5	94.9

Table 4: LIDC lung nodule segmentation (Dice global) and classification (AUC) performance. The 2.5D, I3D and ACS ResNet-18 **p.** are pretrained on ImageNet.

[24] for comparison, all models are adopted a ResNet-18 [26] architecture, except for Model Genesis [72], since the official pretrained model is based on a 3D UNet [11] architecture. For all model training, we use an Adam optimizer [35] with an initial learning rate of 0.001 and train the model for 100 epochs, and delay the learning rate by 0.1 after 50 and 75 epochs. For ResNet-18 backbone, in order to keep higher resolution for output feature maps, we modify the stride of first layer (7×7 stride-2 convolution) into 1, and remove the first max-pooling. Note that this modification still enables pretraining. A FCN-like [42] decoder is applied with progressive upsampling twice. Dice loss with a batch of 8 is used for segmentation, and binary cross-entropy with a batch of 24 for classification. Dice global and AUC are reported for these two tasks. To demonstrate the flexibility and versatility of ACS convolutions, we also report the results of VGG [56] and DenseNet [29] with similar experiment setting in the supplementary materials, which is consistent with the ResNet-18.

Result Analysis. Experiment results are depicted in Table 4. The ACS models consistently outperform all the counterparts by large margins, including 2.5D and 3D models in both random initialization or pretraining settings. P₃SC₁[21]’s performance is similar to standard 3D convolution. We observe that the 3D models (ACS, PSC and 3D) generally outperform the 2.5D models, indicating that the usefulness of 3D contexts. Except for the pretrained 2.5D model on classification task, its superior performance over 3D counterparts may explain the prior art [63,40] with 2D networks on this dataset. As for pretraining, the ImageNet [13] provides significant performance boost (see 2.5D **p.**, 3D **p.** I3D [6] and ACS **p.**), while Med3D [9] brings limited performance boost. We conjecture that it owes to the overwhelming data scale and diversity of 2D image dataset. The segmentation results are visualized in the supplementary materials.

Models	Lesion		Liver	
	Dice Global	Dice per Case	Dice Global	Dice per Case
H-DenseUNet [36]	82.4	72.2	96.5	96.1
Models Genesis [72] ¹	-	-	-	91.13 ±1.51
P ₃ SC ₁ [21] r.	72.3	59.0	93.9	94.2
2.5D DeepLab r.	72.6	56.7	93.1	92.7
2.5D DeepLab p.	73.3	59.8	92.9	92.0
3D DeepLab r.	75.3	62.2	94.8	94.8
3D DeepLab p. I3D [6]	76.4	57.7	94.1	93.4
3D DeepLab p. Med3D [9]	66.8	53.9	92.0	93.6
3D DeepLab p. Video [24]	65.2	55.8	92.5	93.2
ACS DeepLab r.	75.2	62.1	95.0	94.9
ACS DeepLab p.	78.9	65.3	96.7	96.2

Table 5: LiTS segmentation performance. “DeepLab” denotes 3D / ACS ResNet-101 followed by 3D / ACS ASPP block [8]. The 2.5D, I3D and ACS DeepLab **p.** are pretrained on MS-COCO [38].

Due to the difference on network architecture (ResNet-based FCN vs. UNet), we experiment with the official code of self-supervised pretrained Models Genesis [72] with exactly same setting. Even without pretraining, the segmentation and classification performance of the UNet-based models are strong on this dataset. Despite this, the pretrained ACS model is still better performing. Besides, negative transferring is observed for classification experiments by the Models Genesis [72] encoder-only transferring, whereas the ImageNet pretraining consistently improves the performance. Apart from the superior model performance, the ACS model achieves the best parameter efficiency in our experiments. Take the segmentation task for example, the size of ACS model is 49.8 Mb, compared to 49.8 Mb (2.5D), 142.5 Mb (3D) and 65.4 Mb (MG [72]).

4.3 Liver Tumor Segmentation (LiTS) Benchmark

Dataset. We further experiment with our approach on LiTS [5], a challenging 3D medical image segmentation dataest. It consists of 131 and 70 enhanced abdominal CT scans for training and testing respectively, to segment the liver and liver tumors. The training annotations are open to public while the test ones are only accessible by online evaluation. The sizes of x, y axis are 512, while the sizes of z axis vary in the range of [50, 1000]. We transpose the axes into z, y, x to keep the concept consistent as previously mentioned. For pre-processing, we clip the Hounsfield Unit to $[-200, 250]$ and then normalize to $[0, 1]$. Training data augmentation includes random-center cropping, random-axis flipping and rotation, and random-scale resampling.

¹ The author only releases the pretrained model on chest CTs, thereby we simply report the evaluation metric provided by the paper.

	Seg	Cls	Memory (Seg)	Time (Seg)
ACS r.	75.1	92.5	6.6 Gb	0.95 s
M-ACS r.	74.4	89.9	7.8 Gb	1.49 s
S-ACS r.	75.0	89.3	9.9 Gb	1.58 s
ACS p.	76.5	94.9	6.6 Gb	0.95 s
M-ACS p.	75.1	92.7	7.8 Gb	1.49 s
S-ACS p.	75.9	95.1	9.9 Gb	1.58 s

Table 6: A comparison of ACS convolutions and the Mean-ACS and Soft-ACS variants, with / without pretraining, in terms of LIDC segmentation Dice, classification AUC, actual memory and runtime speed per iteration. Memory and time is measured with a batch size of 2, on a single Titan Xp GPU without gradient checkpointing [10]. The memory consuming differs from the theoretical analysis (Table 2) due to PyTorch internal implementation.

Experiment Setting. A DeepLabv3+ [8] with a backbone of ResNet-101 [26] is used in this experiment. The pretrained 2D model is directly obtained from PyTorch’s torchvision package [46]. The compared baselines are similar to those in the above LIDC experiment (Sec. 4.2). We train all the models for 6000 epochs. An Adam optimizer [35] is used with an initial learning rate of 0.001, and we decay the learning rate by 0.1 after 3000 and 4500 epochs. At training stage, we crop the volumes to the size of $64 \times 224 \times 224$. As for testing stage, we crop the volumes to the size of $64 \times 512 \times 512$ and adopt window sliding at a step of 24 at z axis. Dice global and Dice per case of lesion and liver are reported as standard evaluation on this dataset.

Result Analysis. As shown in Table 5, similar model behavior to LIDC experiment (Sec. 4.2) can be observed. The pretrained ACS DeepLab achieves better performance than the 2D and 3D counterparts (including self-supervised pretraining [72]) by large margins; without pretraining, ACS DeepLab achieves comparable or better performance than 3D DeepLab. According to pretraining results on I3D [6], Med3D [9] and Video [24] for 3D DeepLab, negative transferring is observed, probably due to severe domain shift and anisotropy on LiTS dataset. We also report a *state-of-the-art* performance on LiTS dataset using H-DenseUNet[36] as a reference. Note that it adopts a completely different training strategy and network architecture (a heavy cascade of 2D and 3D DenseNet-based [29] models), thereby it is insuitable to compare to our models directly. In further study, it is feasible to integrate these orthogonal contributions into our models to improve the model performance.

5 Ablation Study

5.1 Analysis of ACS Convolution Variants

We analyze the variants of ACS convolutions, including Mean-ACS convolutions and Soft-ACS convolutions. We test these three methods on LIDC-IDRI dataset, using the same experiment settings and training strategy specified in Sec. 4.2. As depicted in Table 6, the vanilla ACS outperforms its variants in most situations, and pretraining is useful in all cases. Specifically, Mean-ACS is the worst under pretraining setting, due to its inability to distinguish the view-based difference with a symmetric aggregation. Soft-ACS outperforms others in some case (*i.e.*, classification with pretraining), though it consumes more GPU memory and time at the training stage. However, it demonstrates the potential to combine these ACS variants or training strategy (*e.g.*, automatic kernel axis assignment).

5.2 Whole-Network vs. Encoder-Only Pretraining

A key advantage of the proposed ACS convolution is that it enables flexible whole-network conversion together with the pretrained weights. We thereby validate the superiority of whole-network weight transferring (WN) over encoder-only weight transferring (EO). We train 4 models in different pretraining setting: entirely randomly-initialized (ACS **r.**), only the pretrained ResNet-101 backbone (ACS **p.EO**) on ImageNet (IMN) [13] and MS-COCO (MSC) [38], and whole pretrained model (ACS **p.WN**). The results are shown in Table 7. It is observed that with more pretrained weights loaded, the model achieves better performance (**p.WN**>**p.EO**>**r.**), and the whole-network pretraining achieves the best. Note that although methods like I3D [6], Med3D [9] and Video [24] provide natively 3D pretrained models, apart from the underperforming performance, these pretraining methods are less flexible and versatile than our method. Generally, only the encoders (backbones) are transferred in previous pretraining methods, however the decoders of *state-of-the-art* models are also very large in parameter size, *e.g.*, the DeepLabv3+ [8] decoder (ASPP) represents 27.5% parameters. The previous pretraining methods hardly take care of the scenarios.

6 Conclusion

We propose ACS convolution for 3D medical images, as a generic and plug-and-play replacement of standard 3D convolution. It enables pretraining from 2D images, which consistently provides significant performance boost in our experiments. Even without pretraining, the ACS convolution is comparable or even better than 3D convolution, with smaller model size and less computation. In further study, we will focus on automatic ACS kernel axis assignment.

Models	Size of Pretrained Weights	Lesion		Liver	
		DG	DPC	DG	DPC
ACS r.	0 Mb (0%)	75.2	62.1	95.0	94.9
ACS p.EO-IMN	170.0 Mb (72.5%)	75.3	64.3	94.7	94.0
ACS p.EO-MS C	170.0 Mb (72.5%)	76.1	61.6	95.5	95.0
ACS p.WN	234.5 Mb (100%)	78.9	65.3	96.7	96.2

Table 7: LiTS segmentation performance of ACS DeepLab “**r.**” (initialized randomly), “**p.EO-IMN**” (encoder-only pretraining on ImageNet [13]), and “**p.EO-MS**C” (encoder-only pretraining on MS-COCO [38]), “**p.WN**” (whole-network pretraining). The model sizes of pretrained weights out of the whole models are also depicted, parameters from the final random initialized layer are not counted.

References

1. Armato III, S.G., McLennan, G., Bidaut, L., McNitt-Gray, M.F., Meyer, C.R., Reeves, A.P., Zhao, B., Aberle, D.R., Henschke, C.I., Hoffman, E.A., et al.: The lung image database consortium (lidc) and image database resource initiative (idri): a completed reference database of lung nodules on ct scans. *Medical physics* **38**(2), 915–931 (2011) [10](#)
2. Balakrishnan, G., Zhao, A., Sabuncu, M.R., Guttag, J., Dalca, A.V.: Voxelmorph: a learning framework for deformable medical image registration. *IEEE transactions on medical imaging* (2019) [1](#)
3. Berthelot, D., Carlini, N., Goodfellow, I., Papernot, N., Oliver, A., Raffel, C.: Mixmatch: A holistic approach to semi-supervised learning. *arXiv preprint arXiv:1905.02249* (2019) [5](#)
4. Bien, N., Rajpurkar, P., Ball, R.L., Irvin, J., Park, A., Jones, E., Bereket, M., Patel, B.N., Yeom, K.W., Shpanskaya, K., et al.: Deep-learning-assisted diagnosis for knee magnetic resonance imaging: development and retrospective validation of mrnet. *PLoS medicine* **15**(11), e1002699 (2018) [1](#)
5. Bilic, P., Christ, P.F., Vorontsov, E., Chlebus, G., Chen, H., Dou, Q., Fu, C.W., Han, X., Heng, P.A., Hesser, J., et al.: The liver tumor segmentation benchmark (lits). *arXiv preprint arXiv:1901.04056* (2019) [1](#), [12](#)
6. Carreira, J., Zisserman, A.: Quo vadis, action recognition? a new model and the kinetics dataset. In: *CVPR*. pp. 6299–6308 (2017) [6](#), [7](#), [8](#), [10](#), [11](#), [12](#), [13](#), [14](#), [25](#)
7. Chen, H., Zheng, Y., Park, J.H., Heng, P.A., Zhou, S.K.: Iterative multi-domain regularized deep learning for anatomical structure detection and segmentation from ultrasound images. In: *International Conference on Medical Image Computing and Computer-Assisted Intervention*. pp. 487–495. Springer (2016) [1](#)
8. Chen, L.C., Zhu, Y., Papandreou, G., Schroff, F., Adam, H.: Encoder-decoder with atrous separable convolution for semantic image segmentation. In: *ECCV*. pp. 801–818 (2018) [3](#), [6](#), [12](#), [13](#), [14](#)
9. Chen, S., Ma, K., Zheng, Y.: Med3d: Transfer learning for 3d medical image analysis. *arXiv preprint arXiv:1904.00625* (2019) [5](#), [8](#), [10](#), [11](#), [12](#), [13](#), [14](#)
10. Chen, T., Xu, B., Zhang, C., Guestrin, C.: Training deep nets with sublinear memory cost. *arXiv preprint arXiv:1604.06174* (2016) [13](#)
11. Çiçek, Ö., Abdulkadir, A., Lienkamp, S.S., Brox, T., Ronneberger, O.: 3d u-net: learning dense volumetric segmentation from sparse annotation. In: *MICCAI*. pp. 424–432. Springer (2016) [2](#), [4](#), [8](#), [9](#), [11](#), [22](#)
12. Dalca, A.V., Balakrishnan, G., Guttag, J., Sabuncu, M.R.: Unsupervised learning for fast probabilistic diffeomorphic registration. In: *MICCAI*. pp. 729–738. Springer (2018) [1](#)
13. Deng, J., Dong, W., Socher, R., Li, L.J., Li, K., Fei-Fei, L.: Imagenet: A large-scale hierarchical image database. In: *CVPR*. pp. 248–255. Ieee (2009) [2](#), [3](#), [5](#), [10](#), [11](#), [14](#), [15](#), [23](#), [25](#)
14. Ding, J., Li, A., Hu, Z., Wang, L.: Accurate pulmonary nodule detection in computed tomography images using deep convolutional neural networks. In: *MICCAI* (2017) [3](#)
15. Dou, Q., Chen, H., Yu, L., Zhao, L., Qin, J., Wang, D., Mok, V.C., Shi, L., Heng, P.A.: Automatic detection of cerebral microbleeds from mr images via 3d convolutional neural networks. *IEEE transactions on medical imaging* **35**(5), 1182–1195 (2016) [1](#)

16. Dou, Q., Yu, L., Chen, H., Jin, Y., Yang, X., Qin, J., Heng, P.A.: 3d deeply supervised network for automated segmentation of volumetric medical images. *Medical image analysis* **41**, 40–54 (2017) [4](#)
17. Droste, R., Cai, Y., Sharma, H., Chatelain, P., Drukker, L., Papageorghiou, A.T., Noble, J.A.: Ultrasound image representation learning by modeling sonographer visual attention. In: *International Conference on Information Processing in Medical Imaging*. pp. 592–604. Springer (2019) [1](#)
18. Esteva, A., Kuprel, B., Novoa, R.A., Ko, J., Swetter, S.M., Blau, H.M., Thrun, S.: Dermatologist-level classification of skin cancer with deep neural networks. *Nature* **542**(7639), 115 (2017) [1](#), [3](#)
19. Fawcett, T.: An introduction to roc analysis. *Pat. Rec. Lett.* **27**(8), 861–874 (2006) [9](#)
20. Gibson, E., Li, W., Sudre, C., Fidon, L., Shakir, D.I., Wang, G., Eaton-Rosen, Z., Gray, R., Doel, T., Hu, Y., et al.: Niftynet: a deep-learning platform for medical imaging. *Computer methods and programs in biomedicine* **158**, 113–122 (2018) [5](#)
21. Gonda, F., Wei, D., Parag, T., Pfister, H.: Parallel separable 3d convolution for video and volumetric data understanding. In: *BMVC* (2018) [4](#), [8](#), [10](#), [11](#), [12](#)
22. Gulshan, V., Peng, L., Coram, M., Stumpe, M.C., Wu, D., Narayanaswamy, A., Venugopalan, S., Widner, K., Madams, T., Cuadros, J., et al.: Development and validation of a deep learning algorithm for detection of diabetic retinopathy in retinal fundus photographs. *Jama* **316**(22), 2402–2410 (2016) [1](#)
23. Han, S., Mao, H., Dally, W.J.: Deep compression: Compressing deep neural networks with pruning, trained quantization and huffman coding. *arXiv preprint arXiv:1510.00149* (2015) [7](#)
24. Hara, K., Kataoka, H., Satoh, Y.: Can spatiotemporal 3d cnns retrace the history of 2d cnns and imagenet? In: *Proceedings of the IEEE conference on Computer Vision and Pattern Recognition*. pp. 6546–6555 (2018) [5](#), [8](#), [10](#), [11](#), [12](#), [13](#), [14](#)
25. He, K., Girshick, R., Dollár, P.: Rethinking imagenet pre-training. In: *CVPR*. pp. 4918–4927 (2019) [5](#)
26. He, K., Zhang, X., Ren, S., Sun, J.: Deep residual learning for image recognition. In: *CVPR*. pp. 770–778 (2016) [6](#), [11](#), [13](#), [23](#)
27. Hénaff, O.J., Razavi, A., Doersch, C., Eslami, S., Oord, A.v.d.: Data-efficient image recognition with contrastive predictive coding. *arXiv preprint arXiv:1905.09272* (2019) [5](#)
28. Hendrycks, D., Lee, K., Mazeika, M.: Using pre-training can improve model robustness and uncertainty. In: Chaudhuri, K., Salakhutdinov, R. (eds.) *ICML. Proceedings of Machine Learning Research*, vol. 97, pp. 2712–2721. PMLR, Long Beach, California, USA (09–15 Jun 2019) [5](#)
29. Huang, G., Liu, Z., Van Der Maaten, L., Weinberger, K.Q.: Densely connected convolutional networks. In: *CVPR*. pp. 4700–4708 (2017) [6](#), [11](#), [13](#), [23](#), [25](#)
30. Hussein, S., Cao, K., Song, Q., Bagci, U.: Risk stratification of lung nodules using 3d cnn-based multi-task learning. In: *International conference on information processing in medical imaging*. pp. 249–260. Springer (2017) [5](#)
31. Irvin, J., Rajpurkar, P., Ko, M., Yu, Y., Ciurea-Ilcus, S., Chute, C., Marklund, H., Haghgoo, B., Ball, R., Shpanskaya, K., et al.: Chexpert: A large chest radiograph dataset with uncertainty labels and expert comparison. In: *AAAI* (2019) [1](#)
32. Isensee, F., Petersen, J., Klein, A., Zimmerer, D., Jaeger, P.F., Kohl, S., Wasserthal, J., Koehler, G., Norajitra, T., Wirkert, S., et al.: nnu-net: Self-adapting framework for u-net-based medical image segmentation. *arXiv preprint arXiv:1809.10486* (2018) [1](#)

33. Johnson, A.E.W., Pollard, T.J., Berkowitz, S., Greenbaum, N.R., Lungren, M.P., Deng, C.y., Mark, R.G., Horng, S.: Mimic-cxr: A large publicly available database of labeled chest radiographs. arXiv preprint arXiv:1901.07042 (2019) [1](#)
34. Kamnitsas, K., Ledig, C., Newcombe, V.F., Simpson, J.P., Kane, A.D., Menon, D.K., Rueckert, D., Glocker, B.: Efficient multi-scale 3d cnn with fully connected crf for accurate brain lesion segmentation. *Medical image analysis* **36**, 61–78 (2017) [4](#), [5](#)
35. Kingma, D.P., Ba, J.: Adam: A method for stochastic optimization. In: *ICLR (2014)* [11](#), [13](#), [23](#)
36. Li, X., Chen, H., Qi, X., Dou, Q., Fu, C.W., Heng, P.A.: H-denseunet: hybrid densely connected unet for liver and tumor segmentation from ct volumes. *IEEE transactions on medical imaging* **37**(12), 2663–2674 (2018) [2](#), [4](#), [12](#), [13](#)
37. Lin, T.Y., Goyal, P., Girshick, R., He, K., Dollár, P.: Focal loss for dense object detection. In: *ICCV*. pp. 2980–2988 (2017) [3](#)
38. Lin, T.Y., Maire, M., Belongie, S., Hays, J., Perona, P., Ramanan, D., Dollár, P., Zitnick, C.L.: Microsoft coco: Common objects in context. In: *ECCV*. pp. 740–755. Springer (2014) [2](#), [5](#), [12](#), [14](#), [15](#)
39. Litjens, G., Kooi, T., Bejnordi, B.E., Setio, A.A.A., Ciompi, F., Ghafoorian, M., Van Der Laak, J.A., Van Ginneken, B., Sánchez, C.I.: A survey on deep learning in medical image analysis. *Medical image analysis* **42**, 60–88 (2017) [1](#)
40. Liu, L., Dou, Q., Chen, H., Qin, J., Heng, P.A.: Multi-task deep model with margin ranking loss for lung nodule analysis. *IEEE transactions on medical imaging* (2019) [11](#)
41. Liu, S., Xu, D., Zhou, S.K., Pauly, O., Grbic, S., Mertelmeier, T., Wicklein, J., Jerebko, A., Cai, W., Comaniciu, D.: 3d anisotropic hybrid network: Transferring convolutional features from 2d images to 3d anisotropic volumes. In: *MICCAI*. pp. 851–858. Springer (2018) [6](#), [7](#)
42. Long, J., Shelhamer, E., Darrell, T.: Fully convolutional networks for semantic segmentation. *CVPR* pp. 3431–3440 (2015) [3](#), [11](#)
43. Menze, B.H., Jakab, A., Bauer, S., Kalpathy-Cramer, J., Farahani, K., Kirby, J., Burren, Y., Porz, N., Slotboom, J., Wiest, R., et al.: The multimodal brain tumor image segmentation benchmark (brats). *IEEE transactions on medical imaging* **34**(10), 1993–2024 (2014) [1](#)
44. Milletari, F., Navab, N., Ahmadi, S.A.: V-net: Fully convolutional neural networks for volumetric medical image segmentation. In: *3DV*. pp. 565–571. IEEE (2016) [2](#), [4](#), [8](#)
45. Ni, T., Xie, L., Zheng, H., Fishman, E.K., Yuille, A.L.: Elastic boundary projection for 3d medical image segmentation. In: *CVPR*. pp. 2109–2118 (2019) [2](#), [3](#)
46. Paszke, A., Gross, S., Chintala, S., Chanan, G., Yang, E., DeVito, Z., Lin, Z., Desmaison, A., Antiga, L., Lerer, A.: Automatic differentiation in PyTorch. In: *NIPS Autodiff Workshop (2017)* [3](#), [10](#), [13](#)
47. Perslev, M., Dam, E.B., Pai, A., Igel, C.: One network to segment them all: A general, lightweight system for accurate 3d medical image segmentation. In: *MICCAI*. pp. 30–38. Springer (2019) [3](#), [4](#)
48. Prasoon, A., Petersen, K., Igel, C., Lauze, F., Dam, E., Nielsen, M.: Deep feature learning for knee cartilage segmentation using a triplanar convolutional neural network. *MICCAI* **16 Pt 2**, 246–53 (2013) [3](#)
49. Qiu, Z., Yao, T., Mei, T.: Learning spatio-temporal representation with pseudo-3d residual networks. *ICCV* pp. 5534–5542 (2017) [4](#)
50. Raghu, M., Zhang, C., Kleinberg, J., Bengio, S.: Transfusion: Understanding transfer learning with applications to medical imaging. In: *NeurIPS (2019)* [5](#)

51. Ronneberger, O., Fischer, P., Brox, T.: U-net: Convolutional networks for biomedical image segmentation. In: International Conference on Medical image computing and computer-assisted intervention. pp. 234–241. Springer (2015) [9](#), [22](#)
52. Roth, H.R., Lu, L., Farag, A., Shin, H.C., Liu, J., Turkbey, E.B., Summers, R.M.: Deeporgan: Multi-level deep convolutional networks for automated pancreas segmentation. In: MICCAI. pp. 556–564. Springer (2015) [1](#)
53. Roth, H.R., Lu, L., Seff, A., Cherry, K.M., Hoffman, J., Wang, S., Liu, J., Turkbey, E., Summers, R.M.: A new 2.5d representation for lymph node detection using random sets of deep convolutional neural network observations. In: Golland, P., Hata, N., Barillot, C., Hornegger, J., Howe, R. (eds.) MICCAI. pp. 520–527. Springer International Publishing, Cham (2014) [2](#), [3](#), [7](#)
54. Setio, A.A.A., Traverso, A., De Bel, T., Berens, M.S., van den Bogaard, C., Cerello, P., Chen, H., Dou, Q., Fantacci, M.E., Geurts, B., et al.: Validation, comparison, and combination of algorithms for automatic detection of pulmonary nodules in computed tomography images: the luna16 challenge. *Medical image analysis* **42**, 1–13 (2017) [2](#)
55. Shen, D., Wu, G., Suk, H.I.: Deep learning in medical image analysis. *Annual review of biomedical engineering* **19**, 221–248 (2017) [1](#)
56. Simonyan, K., Zisserman, A.: Very deep convolutional networks for large-scale image recognition. In: ICLR (2015) [11](#), [23](#), [25](#)
57. Simpson, A.L., Antonelli, M., Bakas, S., Bilello, M., Farahani, K., van Ginneken, B., Kopp-Schneider, A., Landman, B.A., Litjens, G., Menze, B., et al.: A large annotated medical image dataset for the development and evaluation of segmentation algorithms. arXiv preprint arXiv:1902.09063 (2019) [2](#)
58. Sun, R., Limkin, E.J., Vakalopoulou, M., Dercle, L., Champiat, S., Han, S.R., Verlingue, L., Brandao, D., Lancia, A., Ammari, S., et al.: A radiomics approach to assess tumour-infiltrating cd8 cells and response to anti-pd-1 or anti-pd-11 immunotherapy: an imaging biomarker, retrospective multicohort study. *The Lancet Oncology* **19**(9), 1180–1191 (2018) [5](#)
59. Tang, H., Chen, X., Liu, Y., Lu, Z., You, J., Yang, M., Yao, S., Zhao, G., Xu, Y., Chen, T., et al.: Clinically applicable deep learning framework for organs at risk delineation in ct images. *Nature Machine Intelligence* pp. 1–12 (2019) [1](#)
60. Tang, H., Zhang, C., Xie, X.: Nodulenet: Decoupled false positive reduction for pulmonary nodule detection and segmentation. In: MICCAI. pp. 266–274. Springer (2019) [1](#)
61. Wang, X., Peng, Y., Lu, L., Lu, Z., Bagheri, M., Summers, R.M.: Chestx-ray8: Hospital-scale chest x-ray database and benchmarks on weakly-supervised classification and localization of common thorax diseases. In: CVPR. pp. 2097–2106 (2017) [1](#)
62. Xia, Y., Xie, L., Liu, F., Zhu, Z., Fishman, E.K., Yuille, A.L.: Bridging the gap between 2d and 3d organ segmentation with volumetric fusion net. In: MICCAI. pp. 445–453. Springer (2018) [2](#), [4](#)
63. Xie, Y., Xia, Y., Zhang, J., Feng, D.D., Fulham, M., Cai, W.: Transferable multi-model ensemble for benign-malignant lung nodule classification on chest ct. In: MICCAI. pp. 656–664. Springer (2017) [11](#)
64. Yan, K., Peng, Y., Sandfort, V., Bagheri, M., Lu, Z., Summers, R.M.: Holistic and comprehensive annotation of clinically significant findings on diverse ct images: Learning from radiology reports and label ontology. In: CVPR. pp. 8523–8532 (2019) [2](#)

65. Yan, K., Tang, Y., Peng, Y., Sandfort, V., Bagheri, M., Lu, Z., Summers, R.M.: Mulan: Multitask universal lesion analysis network for joint lesion detection, tagging, and segmentation. In: MICCAI. pp. 194–202. Springer (2019) [1](#)
66. Yan, K., Wang, X., Lu, L., Zhang, L., Harrison, A.P., Bagheri, M., Summers, R.M.: Deep lesion graphs in the wild: relationship learning and organization of significant radiology image findings in a diverse large-scale lesion database. In: CVPR. pp. 9261–9270 (2018) [1](#)
67. Yu, Q., Xie, L., Wang, Y., Zhou, Y., Fishman, E.K., Yuille, A.L.: Recurrent saliency transformation network: Incorporating multi-stage visual cues for small organ segmentation. In: CVPR. pp. 8280–8289 (2018) [2](#), [3](#)
68. Zbontar, J., Knoll, F., Sriram, A., Muckley, M.J., Bruno, M., Defazio, A., Parente, M., Geras, K.J., Katsnelson, J., Chandarana, H., et al.: fastmri: An open dataset and benchmarks for accelerated mri. arXiv preprint arXiv:1811.08839 (2018) [2](#)
69. Zhao, W., Yang, J., Sun, Y., Li, C., Wu, W., Jin, L., Yang, Z., Ni, B., Gao, P., Wang, P., et al.: 3d deep learning from ct scans predicts tumor invasiveness of subcentimeter pulmonary adenocarcinomas. *Cancer research* **78**(24), 6881–6889 (2018) [2](#), [4](#)
70. Zheng, H., Zhang, Y., Yang, L., Liang, P., Zhao, Z., Wang, C., Chen, D.Z.: A new ensemble learning framework for 3d biomedical image segmentation. In: AAAI. vol. 33, pp. 5909–5916 (2019) [2](#), [4](#)
71. Zhou, Z., Siddiquee, M.M.R., Tajbakhsh, N., Liang, J.: Unet++: A nested u-net architecture for medical image segmentation. In: Deep Learning in Medical Image Analysis and Multimodal Learning for Clinical Decision Support, pp. 3–11. Springer (2018) [4](#)
72. Zhou, Z., Sodha, V., Siddiquee, M.M.R., Feng, R., Tajbakhsh, N., Gotway, M.B., Liang, J.: Models genesis: Generic autodidactic models for 3d medical image analysis. In: MICCAI. pp. 384–393. Springer (2019) [5](#), [8](#), [11](#), [12](#), [13](#)

Appendix

A Algorithm and Implementation of ACS Convolutions

For the sake of completeness, we describe the detailed calculation of ACS convolutions in Algorithm 1. Besides, we provide a reference implementation in PyTorch (“code.zip”). Actual memory consuming and runtime speed are reported in Table A1. Using the provided function, 2D CNNs could be converted into ACS CNNs for 3D images, with a single line of code.

```

from torchvision.models import resnet18
from acsconv.converters import ACSConverter
# model_2d is a standard PyTorch 2D model
model_2d = resnet18(pretrained=True)
# model_3d is dealing with 3D data
model_3d = ACSConverter(model_2d)

```

Algorithm 1: ACS Convolution

Input: $\mathbf{X}_i \in \mathbb{R}^{C_i \times D_i \times H_i \times W_i}$, $\mathbf{W} \in \mathbb{R}^{C_o \times C_i \times K \times K}$,
padding: \mathbf{p} , stride: \mathbf{s} , dilation: \mathbf{d} , view : $V = \{a, c, s\}$,
kernel split: $(C_o^{(a)}, C_o^{(c)}, C_o^{(s)})$, $\sum_v C_o^{(v)} = C_o$,
pad: compute the padded tensor given a certain axis to satisfy the final output shape same as Conv3D,
unsqueeze: expand tensor dimension given a certain axis.
Output: $\mathbf{X}_o \in \mathbb{R}^{C_o \times D_o \times H_o \times W_o}$

- 1 Compute ACS kernels: $\mathbf{W}_a \in \mathbb{R}^{C_o^{(a)} \times C_i \times K \times K \times 1}$, $\mathbf{W}_c \in \mathbb{R}^{C_o^{(c)} \times C_i \times K \times 1 \times K}$,
 $\mathbf{W}_s \in \mathbb{R}^{C_o^{(s)} \times C_i \times 1 \times K \times K}$
 $\mathbf{W}_a = \text{unsqueeze}(\mathbf{W}[0 : C_o^{(a)}], \text{axis} = a)$;
 $\mathbf{W}_c = \text{unsqueeze}(\mathbf{W}[C_o^{(a)} : C_o^{(a)} + C_o^{(c)}], \text{axis} = c)$;
 $\mathbf{W}_s = \text{unsqueeze}(\mathbf{W}[C_o^{(a)} + C_o^{(c)} :], \text{axis} = s)$;
- 2 Compute view-based 3D features from three views:
for v *in* $V = \{a, c, s\}$ **do**
 $\left[\begin{array}{l} \mathbf{X}_o^{(v)} = \text{Conv3D}(\text{pad}(\mathbf{X}_i, \mathbf{p}, \mathbf{s}, \mathbf{d}, \text{axis} = v), \mathbf{W}_v, \\ \text{stride} = \mathbf{s}, \text{dilation} = \mathbf{d}) \in \mathbb{R}^{C_o^{(v)} \times D_o \times H_o \times W_o}; \end{array} \right.$
- 3 $\mathbf{X}_o = \text{concatenate}([\mathbf{X}_o^{(a)}, \mathbf{X}_o^{(c)}, \mathbf{X}_o^{(s)}], \text{axis} = 0)$.

B Details of Proof-of-Concept Experiment

Dataset. As illustrated in Fig. A1, the synthetic dataset consists of sufficient 2D samples (10,000 for training and 2,000 for evaluation) and limited 3D samples

	Seg	Cls	Memory (Seg)	Time (Seg)
2D r.	68.8	89.4	5.0 Gb	0.57s
3D r.	74.7	90.3	5.0 Gb	1.01 s
ACS r.	75.1	92.5	6.6 Gb	0.95s

Table A1: Model performance, memory consuming and runtime speed of 2D (2.5D) and 3D and ACS convolutions. Due to the engineering issues, the memory of ACS convolutions is large than that of 2D (2.5D) and 3D convolutions, yet theoretically identical (see Table 3). It is expected to be fixed (6.6 Gb to 5.0 Gb) in further implementation by custom memory checkpointing. Even though time complexity of ACS and 2D convolutions is the same, the parallelism of the ACS convolutions is weaker than that of 2D convolutions. Thereby, the actual runtime speed of ACS convolutions is slower than that of 2D convolutions.

(100 for training and 100 for evaluation), in order to validate the usefulness of the proposed method in 2D-to-3D transfer learning. The 2D dataset is for pretraining, which covers 2 foreground classes including circle and square, while the 3D dataset contains 5 foreground classes, including sphere, cube, cylinder, cone and pyramid. Note that the shapes of 2D dataset are exactly the projected single views of 3D volumes (except for triangle), thereby the 2D pretraining should be useful in the 3D segmentation. For both 2D and 3D dataset, the object size, location and direction are randomly assigned, and Gaussian noise is added on each pixel. The input sizes are 48×48 and $48 \times 48 \times 48$ for 2D and 3D dataset.

To generate the 2D dataset, we first equally divide a blank 48×48 2D image into four 24×24 pieces. We randomly choose 3 out of the 4 pieces and in each of the selected piece, we generate a random-size circle or square with same probability at random center. The size is limited in the 24×24 piece. Thereby, the generated shape is guaranteed to be non-overlapped. Similarly, for generating 3D dataset, we equally divide a blank $48 \times 48 \times 48$ 3D volume into eight $24 \times 24 \times 24$ pieces. We randomly choose 4 out of the 8 pieces and in each of the selected piece, we generate a random-size cone, pyramid, cube, cylinder or sphere with same probability at random center. The size is limited in the $24 \times 24 \times 24$ piece. For both 2D and 3D datasets, we add $\mathcal{N}(0, 0.5)$ Gaussian noise on each pixel / voxel. See Fig. A2 for samples of the proof-of-concept 2D and 3D dataset.

Experiment Setting. We compare our ACS model with 2.5D and 3D counterparts under random initialization or pretraining setting. All models share a same UNet [51,11] architecture with down-sampling twice, except for the convolution modules. Dice loss is used for training both 2D and 3D UNet. We first train a 2D UNet on 2D dataset until convergence, which reaches a Dice of 98.57 on 2D dataset. Its weights could be used to transfer to 3D models with ACS convolutions. Note that only 2.5D and ACS UNet are capable of loading the 2D pretrained weights without additional processing. To demonstrate the effect of pretraining for ACS

convolutions, we evaluate the mean AUC (mAUC) between foreground and feature map of final convolution layer without training on the target dataset. The mAUC is obtained by the average of $mean(max(AUC_i, 1 - AUC_i))$ on test set, in which AUC_i is the area under ROC curve of the i th feature channel. Feature values are the predictive values, background is negative ground truth and all foreground classes are the positive ground truth. The reason why we apply $max(AUC_i, 1 - AUC_i)$ is that feature value could be either large or small to be “activated”. For training on 3D dataset, We apply an Adam optimizer [35] with 0.001 learning rate and train models for 50 epochs with a batch size of 4. We report the macro-averaged Dice and mIoU of 3D dataset.

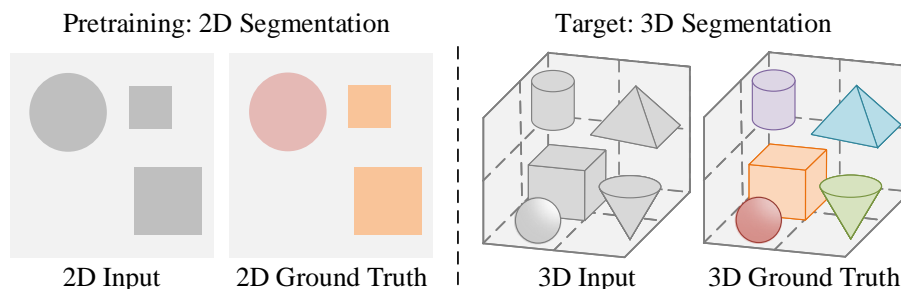


Fig. A1: Illustration of the proof-of-concept dataset in this study to perform 3D segmentation with 2D pretraining.

C More Results on LIDC-IDRI

Apart from the ResNet [26], we further experiment with the proposed ACS convolutions on LIDC-IDRI lung nodule classification and segmentation task, using VGG [56] and DenseNet [29]. The experiment settings are exactly the same with ResNet-18, which is stated in the Sec. 4.2. As depicted in Table A2 and A3, the results are consistent with the ResNet-18 performance. The 3D (3D and ACS) models outperform the 2D (2.5D) ones. The randomly-initialized ACS models are comparable or better than the 3D models; when pretrained with 2D datasets (*e.g.*, ImageNet [13]), the ACS models consistently outperform the 3D ones.

D Qualitative Results on Nodule Segmentation

We visualize the segmentation masks generated by the 2.5D, 3D and ACS ResNet-18, with or without pretraining in Fig. A3. Combined the visualization with overall performance (Table 5), ACS **p**. segment the target nodules more precisely than other counterparts in general.

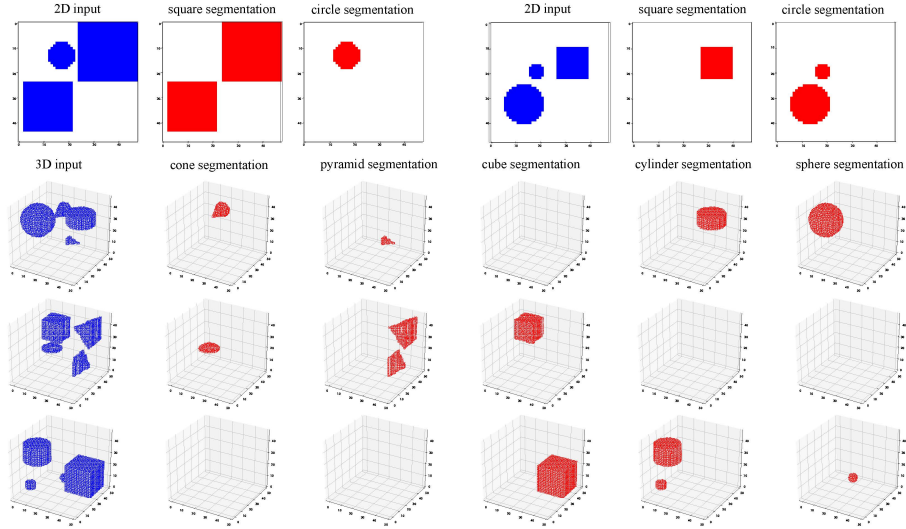


Fig. A2: Samples of the proof-of-concept 2D and 3D datasets. Images in the first row are two 2D samples, while those in the next three rows are three 3D samples. Images with blue figures are input (before adding noise), while images with red figures are target segmentations.

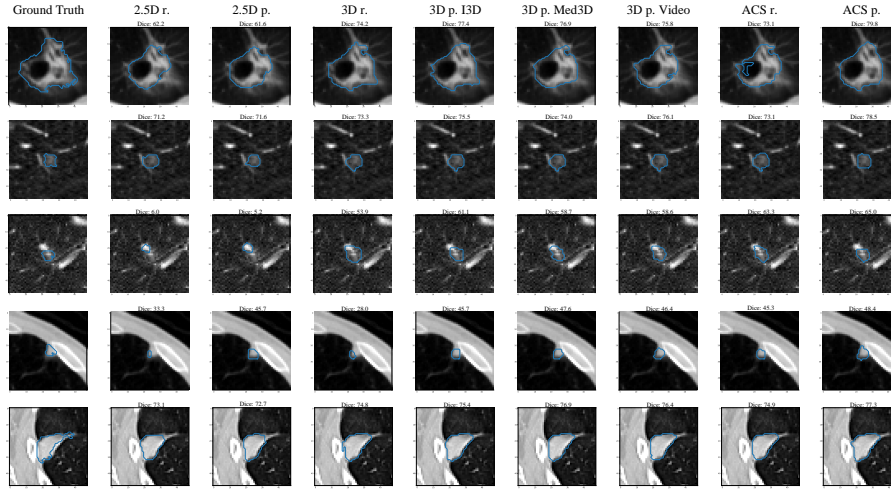


Fig. A3: Visualization of the segmentation masks generated by the 2.5D, 3D and ACS ResNet-18, with or without pretraining. The number on top of each image indicates the Dice per case of the sample.

Models	Segmentation	Classification
2.5D VGG-16 r.	71.0	89.7
2.5D VGG-16 p.	71.6	93.9
3D VGG-16 r.	75.0	91.7
3D VGG-16 p. I3D [6]	75.5	94.0
ACS VGG-16 r.	75.2	94.2
ACS VGG-16 p.	75.8	94.3

Table A2: VGG-16 [56] results on LIDC lung nodule segmentation (Dice global) and classification (AUC) performance. The 2.5D, I3D and ACS VGG-16 **p.** are pretrained on ImageNet [13].

Models	Segmentation	Classification
2.5D DenseNet-121 r.	67.4	87.4
2.5D DenseNet-121 p.	71.8	92.6
3D DenseNet-121 r.	73.6	90.0
3D DenseNet-121 p. I3D [6]	73.6	90.0
ACS DenseNet-121 r.	73.4	89.2
ACS DenseNet-121 p.	74.7	92.9

Table A3: DenseNet-121 [29] results on LIDC lungs on nodule segmentation (Dice global) and classification (AUC) performance. The 2.5D, I3D and ACS DenseNet-121 **p.** are pretrained on ImageNet [13].